

PERTURBATION THEORY IN THE DESIGN OF DEGENERATE RECTANGULAR DIELECTRIC RESONATORS

L. K. Warne, L. I. Basilio^{*}, W. L. Langston, W. A. Johnson, and M. B. Sinclair

Sandia National Laboratories, Electromagnetic Theory, P. O. Box 5800, Albuquerque, NM 87185-1152, USA

Abstract—The design of resonators with degenerate magnetic and electric modes usually requires the ability to perturb one or both types of modes in order to induce alignment of magnetic and electric properties. In this paper perturbation theory is used to identify different types of inclusions that can be used to realize fundamental-mode degeneracy in a rectangular dielectric resonator and thus, can ultimately be used in the design of negative-index metamaterials. For reasons associated with fabrication in the infrared-frequency regime, rectangular resonator designs are of particular interest.

1. INTRODUCTION

Metamaterials based on resonant-cell structures are often used to obtain a negative index of refraction, where both the effective permittivity and permeability are negative, and operation is adjusted to occur just above (in frequency) spectrally overlapping magnetic and electric resonances of the cell structures [1]. Other applications of metamaterials, including cloaking, require independent tuning of the permittivity and permeability and thus require the ability to place the resonances at the desired spectral positions. In addition to the selective placement of resonances, remaining in the effective material limit (with diffraction suppressed [2–6]) is another goal in these types of metamaterial applications. Often times unit cells containing metallic split-ring resonators (yielding the magnetically-resonant component [7]) and loaded dipoles (yielding the electrically-resonant component [8–10]) are used in constructing negative-index metamaterials since they can be small and still attain both negative

Received 16 July 2012, Accepted 23 August 2012, Scheduled 12 September 2012

^{*} Corresponding author: Lorena I. Basilio (libasil@sandia.gov).

permittivity and permeability. In these cases, tuning of the electric and magnetic resonances is achieved through the design of the respective resonators. In another approach, core-shell nanoclusters (including metal cores), which are compatible with self-assembly technologies, have also been explored as a means of realizing a double-negative medium in the visible range [11].

In recent years, all-dielectric resonant structures utilizing high-permittivity materials have drawn much attention since their use reduces the material absorption inherent to metallic structures (which can become prohibitive at higher frequencies [11]). While dielectric cylinders and rectangles have frequently been used to realize a medium of negative-permeability [12–14], all-dielectric resonators are not a natural fit for negative-index applications, since the first magnetic resonance occurs at a lower frequency than the first electric resonance.

Well-known approaches that have been used to attempt to align the resonances of all-dielectric resonators include the core-shell designs of [15, 16] and the AB-type designs of [17, 18]. While both of these methods introduce an additional degree of freedom that provides for the tuning of the resonances (in [15, 16] by introducing a surrounding dielectric shell layer to a dielectric core and in [17, 18] by introducing an additional resonator particle into the unit cell), unfortunately these two approaches can easily bring into question the applicability of effective media; this becomes particularly apparent at higher operating frequencies. In the case of the AB-type design, the size of the unit cell is physically extended (perhaps by a factor of two) to accommodate the additional resonator while, alternatively, in the core-shell design the electrical size of the resonator is forced to increase because overlap of only higher-order modes is possible. As the operating frequency is increased, an additional problem that arises in both these approaches (and any other all-dielectric designs) is that the range of available permittivities becomes much more limited. For example, in the long-wave infrared ($8\ \mu\text{m}$ – $15\ \mu\text{m}$) the largest relative permittivities available in low-loss dielectric materials are in the range of 25–32 [19], while relative permittivities in the hundreds (or higher) are common at radio frequencies. To achieve resonance and still remain in the effective medium limit then becomes a difficult proposition. Nevertheless, as metamaterial designs are pushed to higher frequencies, the need for dielectric resonators is imperative since absorption associated with the metallic resonators becomes significant. Any methods based on dielectric resonators where degeneracy of the lowest-order magnetic and electric-resonant modes is realized and which consequently do not increase the lattice spacing become especially appealing.

This paper discusses different types of perturbations that can be

made within a single rectangular dielectric resonator for the purpose of changing the spectral positions of the lowest magnetic and electric resonant modes. The lowest modes are selected in order to keep the resonator as electrically small as possible. (In [20], a similar approach is presented for spherical dielectric resonators.) Here we focus on rectangular resonators since infrared is the frequency band of interest and these resonators are easier to fabricate by lithographic techniques in this frequency range (as in the visible band). Several microwave-frequency designs utilizing perturbed dielectric sphere resonators are presented in [21].

Included in this paper are the frequencies and field distributions for rectangular dielectric resonators found through a waveguide approximation, as well as through numerical simulations. Perturbation theory is introduced for design purposes since it can be used to arrive at approximate predictions for the modal shifts (in terms of frequency or wavelength) realized with particular inclusions. Although resonator designs demonstrating modal degeneracy (which can be used for the construction of negative-index metamaterials) at infrared wavelengths will be the focus of this paper, our approach can also be used to tune the spectral locations of the modes to achieve other desired combinations of effective permittivity and permeability.

2. DIELECTRIC RESONATORS

The modes of dielectric resonators are typically interlaced in frequency, with the lowest magnetic resonance occurring before (lower frequency) the lowest electric resonance. In this paper we treat the rectangular resonators as isolated (corresponding to lower packing fractions in the periodic lattice) and discuss the effects of the periodic lattice where appropriate. Throughout the paper we consider PbTe dielectric resonators at infrared frequencies where the relative permittivity is given by $\varepsilon_r = 32.04 + i0.0566$ (where $\varepsilon_r = \varepsilon/\varepsilon_0$ and $\varepsilon_0 = 8.854188$ pF/m is the free space permittivity) [19]. (For simplicity in the theoretical analysis, we consider only the real part of the PbTe permittivity.) All simulations are generated using an integral-equation, method-of-moments code called EIGERTM [22].

2.1. Boundary Value Problem

In this section we briefly discuss the global and local coordinate systems used in the modeling and review the boundary conditions associated with the use of high-contrast materials inside the resonators.

2.1.1. Coordinate Systems

It is convenient to use a global coordinate system for the incident plane wave and the array of particles, and two local coordinate systems attached to a single particle. The global system has x in the direction of the incident magnetic field, y in the direction of the incident electric field, $-z$ in the direction of the incident wavevector \underline{k}_0 (direction of the incident wave), and the origin will be taken at the center of one particle. This global coordinate system is used in all the simulations that follow.

Since the modes in the resonators naturally separate into transverse electric (TE) and transverse magnetic (TM), in the theoretical analysis it is convenient to use two local coordinate systems where the z axis is aligned with the direction of the incident magnetic field (TE), or alternatively with the incident electric field (TM). These local coordinates are used in the sections where the modal fields and the inclusions are discussed. These sections use a , b , and c , for the half dimensions of the rectangular resonator along the local x , y , and z directions, respectively, and do not permute the dimensions (which would have to be done for a rectangular geometry to make the link to the global coordinate system); this approach is taken since we are primarily interested in a cubic resonator.

2.1.2. High-contrast Conditions

For the resonator geometry shown in Fig. 1, the continuity of the normal displacement $\varepsilon_2 E_{2n} = \varepsilon_1 E_{1n}$ and tangential electric field intensity $E_{2t} = E_{1t}$ at the resonator boundary imply that the exterior

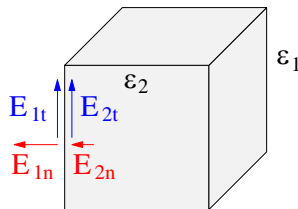


Figure 1. The exterior and interior electric fields at the resonator boundary, corresponding to regions of permittivity ε_1 and ε_2 respectively, can be used to obtain the energy just outside and inside of the resonator.

electric energy density at the boundary is

$$w_e^{ex} = \frac{1}{2}\varepsilon_1 E_1^2 = \frac{1}{2}\varepsilon_1 (E_{1n}^2 + E_{1t}^2) = \frac{1}{2}\varepsilon_2 \left[\left(\frac{\varepsilon_2}{\varepsilon_1} \right) E_{2n}^2 + \left(\frac{\varepsilon_1}{\varepsilon_2} \right) E_{2t}^2 \right] \quad (1)$$

whereas the interior energy density is

$$w_e^{in} = \frac{1}{2}\varepsilon_2 E_2^2 = \frac{1}{2}\varepsilon_2 (E_{2n}^2 + E_{2t}^2) \quad (2)$$

Thus, the exterior electric energy density for the tangential field part is $O(\varepsilon_1/\varepsilon_2)$ of the interior, but the normal field part is $O(\varepsilon_2/\varepsilon_1)$ of the interior. For a confined mode we expect the energy to be concentrated on the interior and therefore we would anticipate that $E_{2n}/E_{2t} \rightarrow 0$ as a wall is approached. This corresponds to the condition we would expect at the surface of a perfect magnetic conductor (PMC). We can apply this condition on the electric field but we must remember that the normal magnetic field will penetrate the walls of the resonator [23, 24]. Furthermore, as described in [23, 24], the application of PMC boundary conditions to the tangential magnetic field (for example, in the case of the magnetic mode) is generally not correct.

2.2. Rectangular Dielectric Resonators

The goal of this section is to theoretically characterize the two lowest-order modes associated with a rectangular dielectric resonator. Numerical simulations are also presented as verification to the theoretical predictions. As previously discussed, rectangular dielectric resonators are of particular interest in the infrared and visible frequency range since they are easier to fabricate lithographically.

2.2.1. Waveguide Method for First Magnetic Mode

An approximate treatment of these resonators is based on using waveguide extensions of the resonator in one direction, as in [25]. The local coordinate system is being used where z is along the magnetic field and transverse to the electric field. The first magnetic mode is an open form of the PMC mode TE_{110}^z often denoted by $TE_{11\delta}^z$ with fields

$$\underline{H} = \nabla (\nabla \cdot \underline{\Pi}_m) + k^2 \underline{\Pi}_m \quad (3)$$

$$\underline{E} = i\omega\mu_0 \nabla \times \underline{\Pi}_m \quad (4)$$

and potential

$$\underline{\Pi}_m = \psi_m \underline{e}_z \quad (5)$$

$$(\nabla^2 + k^2)\psi_m = 0 \quad (6)$$

For a dielectric resonator of dimensions $2a$, $2b$, $2c$ with $-a < x < a$, $-b < y < b$, $-c < z < c$ the potential of the $TE_{11\delta}^z$ mode is taken as

$$\psi_m = A \cos(k_x x) \cos(k_y y) \cos(k_z z) \quad (7)$$

for the interior region and

$$\psi_m = A \cos(k_x x) \cos(k_y y) \cos(k_z c) e^{ik_{1z}(|z|-c)} \quad (8)$$

for the exterior region (here we have matched the normal magnetic field for the case of nonmagnetic materials). The relationship between wavenumbers is given by

$$k^2 - k_z^2 = k_x^2 + k_y^2 = k_t^2 = k_1^2 - k_{1z}^2 \quad (9)$$

where $k = \omega\sqrt{\mu_0\varepsilon_2}$ is the wavenumber inside the dielectric cavity, $k_1 = \omega\sqrt{\mu_0\varepsilon_1}$ the wavenumber in the host media, and k_t the transverse wavenumber. In the case of PMC side walls we must have $E_x(x = \pm a) = 0 = E_y(y = \pm b)$ and $H_x(y = \pm b) = 0 = H_y(x = \pm a)$ which hold for $k_x = \pi/(2a)$ and $k_y = \pi/(2b)$. Matching the tangential field at the $z = c$ interface gives

$$k_z \tan(k_z c) = -ik_{1z} \quad (10)$$

where eliminating k_{1z} gives

$$k_z c = \arctan \sqrt{k_t^2 (1 - \varepsilon_1/\varepsilon_2) / k_z^2 - \varepsilon_1/\varepsilon_2} \quad (11)$$

Thus, for $\varepsilon_2/\varepsilon_1 = 32$ and the limiting case of a cube where $a = b = c$ we find that $k_z c \approx 1.10225$ (or $k_z \approx 0.7017\pi/(2c)$). This corresponds to a resonant interior wavenumber of $k_{11\delta} \approx \pi\sqrt{2.49}/(2c)$. For the case of $b \rightarrow b/2$, we have $(k_t c)^2 \rightarrow \pi^2(5/4)$ and $k_z c \approx 1.2287$ (or $k_z \approx 0.7822\pi/(2c)$) and resonant wavenumber $k_{11\delta} \approx \pi\sqrt{5.61}/(2c)$. This waveguide method is not extremely accurate for this range of aspect ratios, but is nevertheless useful (in the next paragraph it is compared to the first resonance that is observed in the numerical simulations).

Figure 2 shows the simulation result (using the global coordinate system) for the magnetic field (H_x) distribution within a dielectric cube with $\varepsilon_r = \varepsilon_2/\varepsilon_1 = 32$ and $2a = 1.53\ \mu\text{m}$ at a resonant wavelength of $10.57\ \mu\text{m}$ and $k_y = k_z \approx 1.06\pi/(2a)$, as well as $k_x \approx 0.68\pi/(2a)$. This numerical simulation result is obtained by employing a symmetric magnetic excitation of an isolated dielectric cube as described in [10]. We note that the normalized simulated wavenumber (0.68) in the direction of the incident magnetic field is close to the one-dimension waveguide prediction of 0.70. In Fig. 3 the simulated electric field distributions along the y and z directions of the PbTe cube are presented and clearly illustrate the near-magnetic wall

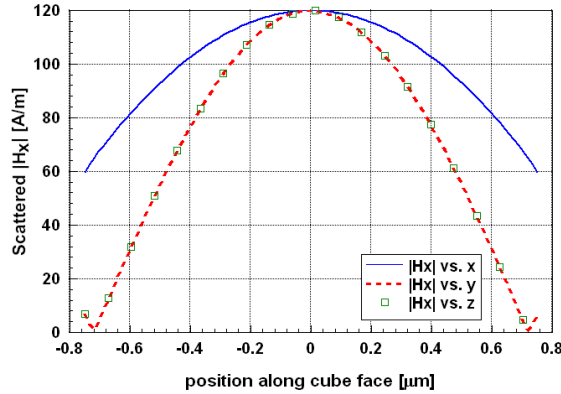


Figure 2. Magnitude of the scattered H_x along the x , y , and z -dimensions of a PbTe cubic resonator (centered about the origin) of side length $1.53 \mu\text{m}$. The fields are sampled at an operating wavelength of $10.57 \mu\text{m}$ and along the $y = z = 0$; $x = z = 0$; and $x = y = 0$ planes, respectively.

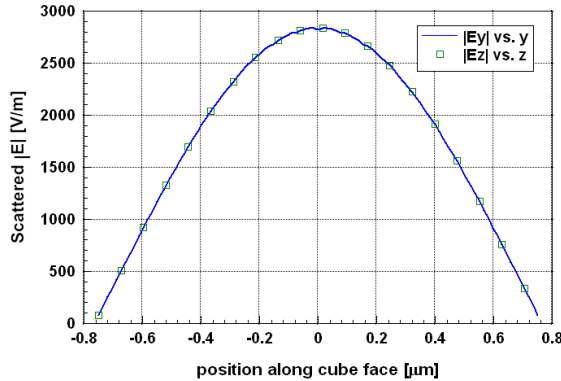


Figure 3. Magnitude of the scattered E_y and E_z along the y and z -dimensions of a PbTe cubic resonator (centered about the origin) of side length $1.53 \mu\text{m}$. The fields are sampled at an operating wavelength of $10.57 \mu\text{m}$ and along the $x = 0, z = 0.765 \mu\text{m}$; and $x = 0, y = 0.765 \mu\text{m}$ planes, respectively.

(PMC) behavior. Note that the interior fields shown are total fields (the incident field is relatively small at 1 A/m from each of the two directions, and is in approximate phase quadrature with the resonant

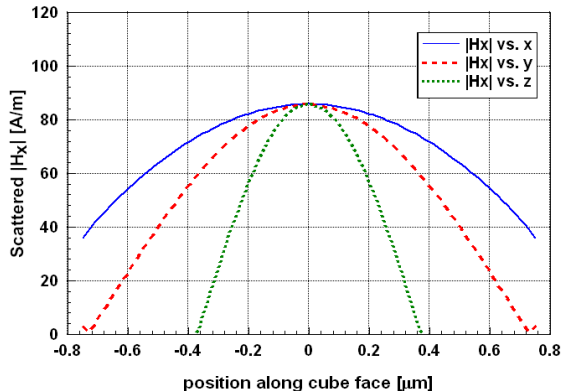


Figure 4. Magnitude of the scattered H_x along the x , y , and z -dimensions of a PbTe cubic resonator (centered about the origin) of side lengths $a = b = 1.53 \mu\text{m}$, and $c = 0.765 \mu\text{m}$. The fields are sampled at an operating wavelength of $7.17 \mu\text{m}$ and along the $y = z = 0$; $x = z = 0$; and $x = y = 0$ planes, respectively.

response).

The interior magnetic field generated by a symmetric excitation [10] of a single PbTe half-cube resonator with the reduced dimension occurring in the direction of propagation ($2b \rightarrow a$ in the local coordinate system, but $2c \rightarrow a$ in the global coordinate system) is shown in Fig. 4. The simulated resonance is found to occur at $7.17 \mu\text{m}$ and $k_x \approx 0.75\pi/(2a)$. Thus, the normalized wavenumber in the magnetic field direction (0.75) is near the waveguide prediction of 0.78.

2.2.2. First Electric Mode

Here the local coordinate system is being used where z is now along the electric field and transverse to the magnetic field. The first electric mode is taken to be an open form of TM_{111}^z with fields

$$\underline{E} = \nabla(\nabla \cdot \underline{\Pi}_e) + k^2 \underline{\Pi}_e \quad (12)$$

$$\underline{H} = -i\omega\varepsilon \nabla \times \underline{\Pi}_e \quad (13)$$

and potential

$$\underline{\Pi}_e = \psi_e \underline{e}_z \quad (14)$$

$$(\nabla^2 + k^2)\psi_e = 0 \quad (15)$$

We take the potential to consist of approximately

$$\psi_e = A \cos(k_x x) \cos(k_y y) \cos(k_z z) \quad (16)$$

Note that if near-PMC boundary conditions [23] are imposed on the boundary, we expect that $k_z \approx \pi/(2c)$. We denote the first mode by $TM_{\xi\zeta 1}^z$ with $\xi > 1$ and $\zeta < 2$, where $k_x = \xi\pi/(2a)$ and $k_y = \zeta\pi/(2b)$.

For the case where $a = b = c$, we have observed from the numerical simulation that $\xi \approx \zeta \approx 1.4 \approx \sqrt{2}$ and a cutoff wavelength in the cube corresponding to $k_{\xi\zeta 1} \approx \pi\sqrt{5}/(2a)$ is realized. Fig. 5 shows the E_y field distribution (again using a symmetric electric excitation [10] of a single resonator via EIGERTM) along selected planes in a PbTe cubic resonator of side length $s = 1.53 \mu\text{m}$. In the simulations the global coordinate system is used and the mode of interest is $TM_{\zeta 1 \xi}^y$.

2.2.3. Results for the Unperturbed Rectangular Resonator

It is important to note that while the spectral locations of the resonances determined from a single-particle simulation are directly correlated with the transmission coefficient associated with a periodic assembly of the resonators (an example of this is shown in the next section), a simulation of an isolated resonator is being used here for the purposes of also identifying the nature of the resonance (electric versus magnetic and dipole versus quadrupole). This additional information (together with the resonant wavelength) is key in moving towards a degenerate resonator design with overlapping lowest-order magnetic and electric resonances and which ultimately demonstrates negative-

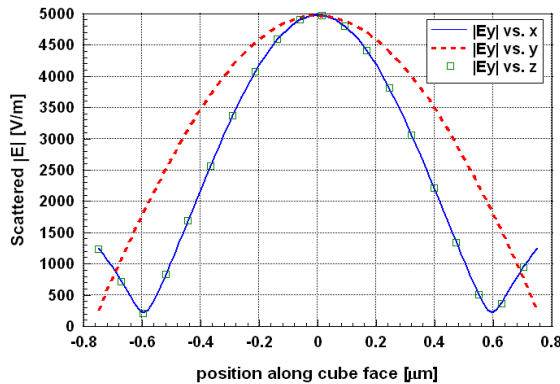


Figure 5. Magnitude of the scattered E_y along the x , y , and z -dimensions of a PbTe cubic resonator (centered about the origin) of side length $1.53 \mu\text{m}$. The fields are sampled at an operating wavelength of $7.83 \mu\text{m}$ and along the $y = z = 0$; $x = z = 0$; and $x = y = 0$ planes, respectively.

index behavior.

In general, the far-zone radiation patterns of the isolated resonator can be used to extract the magnetic (in the local coordinates $M_{zz} \rightarrow M_{xx}$ in the global coordinates) and electric (in the local coordinates $P_{zz} \rightarrow P_{yy}$ in the global coordinates) polarizabilities and ultimately determine the constitutive parameters describing an effective media comprised of an infinite array of these resonators [10]. That is, for a periodic arrangement of resonators the effective permeability and permittivity by means of the Clausius-Mossotti relation are

$$\mu_{eff}/\mu_0 = \mu_{reff} = 1 + \frac{n_d M_{zz}}{1 - n_d M_{zz}/3} \quad (17)$$

and

$$\varepsilon_{eff}/\varepsilon_1 = \varepsilon_{reff} = 1 + \frac{n_d P_{zz}}{1 - n_d P_{zz}/3} \quad (18)$$

where $n_d = 1/d^3$ is the packing density of the resonators in a periodic cubic lattice with spacing d [1]. Thus, for the simulations, a single resonator excited with the plane-wave orientation shown in Fig. 6 is considered. (To facilitate the interpretation of the response, a superposition of plane waves is set up to create a cancellation of either the electric or magnetic field at the center of the resonator [10].) Following the same procedure as described in [10] and implemented in [21], the resonant wavelengths are determined by the peaks in the far-zone scattered fields generated by the isolated resonator. The results for a PbTe cubic resonator of side length $s = 1.53 \mu\text{m}$ are shown in Fig. 7 (sampled on the $\theta = 90^\circ$ plane for $\phi = 0^\circ$ and 90°), where peaks in the far-field amplitude (for the isolated particle) are seen to occur at $10.6 \mu\text{m}$, $7.8 \mu\text{m}$, and $7.0 \mu\text{m}$.

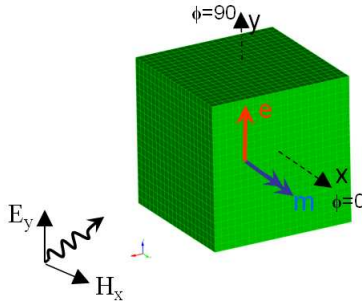


Figure 6. Coordinate system and excitation used in the rectangular resonator simulations.

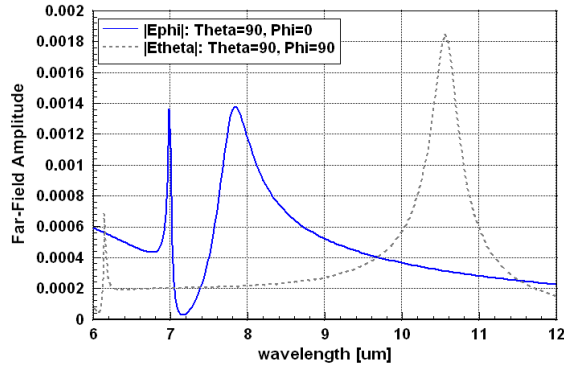


Figure 7. Radiated far-field amplitudes of a single PbTe ($\epsilon_r = 32.04 + i0.0566$) cubic resonator of side length $1.53 \mu\text{m}$. Sampling positions are located on the $\theta = 90^\circ$ plane at $\phi = 0^\circ$ and 90° .

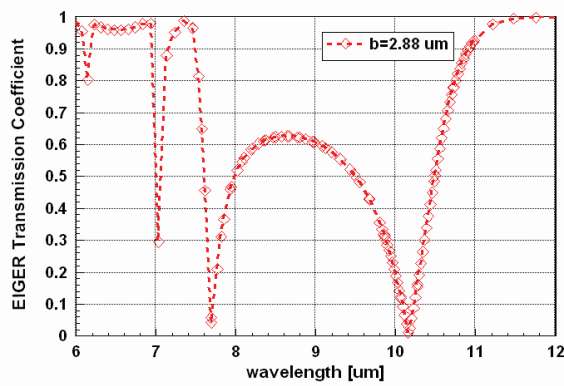


Figure 8. Transmission coefficient for an array of PbTe cubic resonators (of side length $1.53 \mu\text{m}$) with period $2.88 \mu\text{m}$.

Figure 8 shows the transmission coefficient for a periodic array (single layer) of PbTe cubic resonators arranged with a volume-packing fraction of 0.15. Here the minima of the transmission coefficient are seen to occur at wavelengths in the vicinity of those yielding peaks in the far-field amplitudes shown in Fig. 7. (Note that due to the periodic loading the magnetic resonance is slightly shifted in position relative to the isolated resonator case.)

As in [10, 20, 21], we use the far-field scattered patterns to extract the dipole moments of the isolated resonator. The scattered patterns sampled at each of the wavelengths identified from Fig. 7 are plotted in Fig. 9. These pattern results are used to extract the effective-

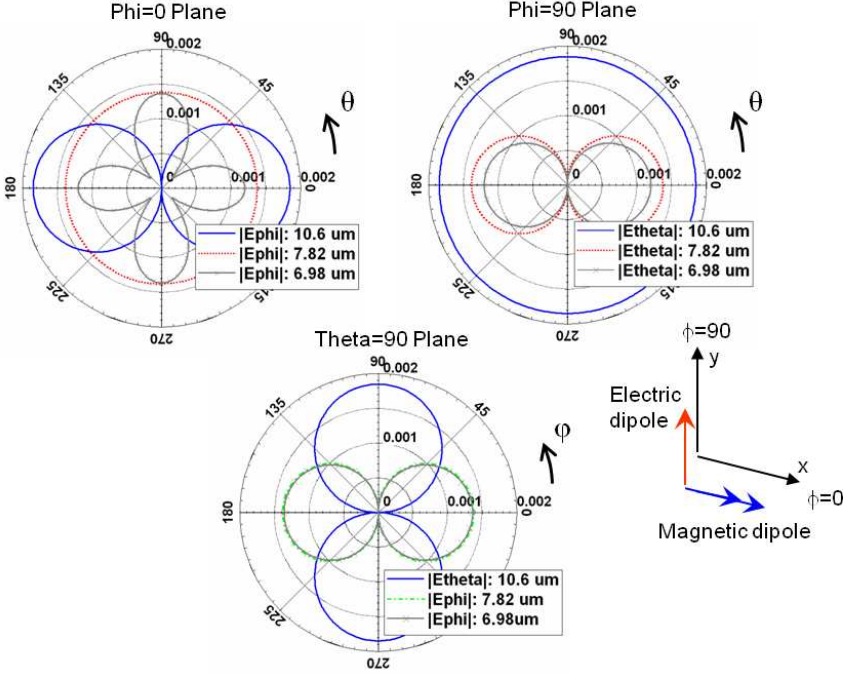


Figure 9. The radiation patterns associated with a cubic PbTe resonator at each of the peak frequencies determined from the results in Fig. 7. In order of decreasing wavelength, the radiation patterns indicate that a magnetic dipole, electric dipole, and magnetic quadrupole characterize the cubic resonator within this spectral band.

media parameters ((17), (18)), shown in Fig. 10, for a cubic array of PbTe cubes ($s = 1.53 \mu\text{m}$) with period $3.30 \mu\text{m}$. Here we note that the magnetic dipole as well as the electric-dipole resonances are clearly indicated in the effective permittivity and permeability response (the quadrupole effect at $7 \mu\text{m}$ is due to the single-point polar sampling used to approximately determine the dipole moments [10]). In addition, the spectral locations for the effective-media resonances are nicely correlated with the single-particle simulations.

It is the goal of the next section to manipulate the cavity-field structures (via perturbations) of the cubic dielectric resonator so that overlapping lowest-order electric and magnetic modes is achieved. With this type of single-resonator degenerate design, a metamaterial design realizing negative-index behavior and satisfying effective-media constraints is made more accessible.

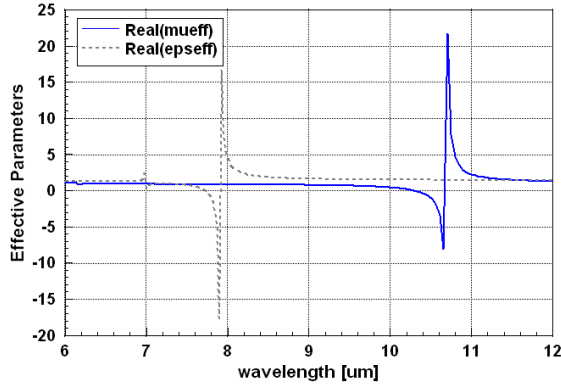


Figure 10. The extracted effective permeability and permittivity (relative to free space) for a PbTe cube of side length $1.53 \mu\text{m}$. For simplicity, only the real parts of the effective parameters are shown.

3. PERTURBATION APPROACH

From Maxwell’s equations for a dielectric resonator with permittivity function ε operating at frequency ω_0 and a resonator with a small perturbation ε_p operating at frequency $\omega_0 + \delta\omega$ we find

$$\begin{aligned}
 & - \oint_S (\underline{E} \times \underline{H}_0^* + \underline{E}_0^* \times \underline{H}) \cdot \underline{n} dS \\
 & = -i\omega_0 \int_{V_p} (\varepsilon_p - \varepsilon) \underline{E}_0^* \cdot \underline{E} dV - i(\delta\omega) \int_V (\varepsilon \underline{E} \cdot \underline{E}_0^* + \mu_0 \underline{H} \cdot \underline{H}_0^*) dV \quad (19)
 \end{aligned}$$

where \underline{E}_0 and \underline{H}_0 are the unperturbed fields. V is the resonator volume (including a region outside the resonator where the interior fields have penetrated), S the closed surface bounding the volume V , \underline{n} the outward pointing unit vector on S , ε the permittivity function inside and outside the resonator ($\varepsilon \rightarrow \varepsilon_1$ outside) and here assumed to be real, and ε_p the value in the perturbation contained in volume V_p . Since we will ignore the effect of radiation (approximating the exterior as quasistatic), the surface integral in (19) can be dropped. Approximating the fields in the perturbed resonator by the unperturbed fields $\varepsilon \underline{E} \cdot \underline{E}_0^* \approx \varepsilon \underline{E}_0 \cdot \underline{E}_0^*$ and $\mu_0 \underline{H} \cdot \underline{H}_0^* \approx \mu_0 \underline{H}_0 \cdot \underline{H}_0^*$ throughout most of the cavity volume (and the local exterior) in the second term, we arrive at the typical formula

$$- \frac{\delta\omega}{\omega_0} \approx \frac{\int_{V_p} (\varepsilon_p - \varepsilon) \underline{E}_0^* \cdot \underline{E}_p dV}{\int_V (\varepsilon \underline{E}_0 \cdot \underline{E}_0^* + \mu_0 \underline{H}_0 \cdot \underline{H}_0^*) dV} \approx \frac{\int_{V_p} (\varepsilon_p - \varepsilon) \underline{E}_0^* \cdot \underline{E}_p dV}{2 \int_V \varepsilon \underline{E}_0 \cdot \underline{E}_0^* dV} \quad (20)$$

[26]. The final formula on the right makes use of the equivalence of the magnetic and electric energies stored in the resonator and the field in the perturbation ε_p is denoted by \underline{E}_p . If ε_p is complex the inclusion is lossy; thus, care should be taken to choose materials with low loss since the field may be magnified in this region. Note that to treat absorption in the resonator material ε we remove the conjugates in the final expression on the right [26] (with only electric field terms). This expression provides us with the means to estimate the frequency shift from the inclusion properties.

3.1. Inclusions and Placement

One approach to alignment of resonances is to place perturbations within the resonator volume in an effort to perturb the resonant frequencies into alignment. It is useful to select polarization-dependent perturbations of high contrast relative to the resonator material so that one of the modes is selected (by virtue of the associated field orientation) and the respective resonant frequency is shifted in the appropriate direction. High-permittivity inclusions can be realized with metallic dipoles which are oriented along electric field lines associated with the first excited electric mode (and ideally at a null of the electric field of the first magnetic mode) as shown in Fig. 11. This type of perturbation has the effect of shifting the electric resonance downward in frequency toward the first magnetic mode. Whereas we are using these inclusions to obtain single-particle degeneracy (as in [20, 21] for spherical resonator designs), it should be noted that inclusions of this type have been used previously to establish gradient properties for a lens design [27].

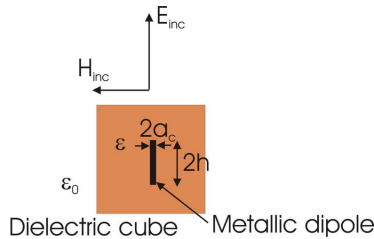


Figure 11. In order to realize a frequency downshift in the electric resonance (towards the magnetic resonance), a metallic dipole is embedded within the dielectric resonator (the outer medium in this figure has $\varepsilon_1 = \varepsilon_0$). A cubic dielectric resonator is shown as an example, where the dipole is oriented along the direction of the incident electric field.

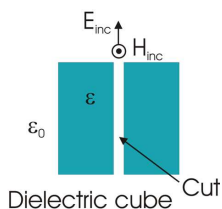


Figure 12. A split (or cutout) along the center of the dielectric resonator can be introduced to upshift (in frequency) the magnetic resonance towards the higher-frequency electric resonance. A cubic resonator is shown as an example, where the cut plane is positioned to contain both the electric and magnetic incident field (here the outer medium and the perturbation cutout have $\varepsilon_1 = \varepsilon_0 = \varepsilon_p$).

Alternatively, low-permittivity inclusions can be realized by splits (or cuts), filled with gas or other low-permittivity materials, oriented perpendicular to electric field lines associated with the lowest magnetic mode (and ideally having no normal electric field from the first electric mode). With the type of perturbation shown in Fig. 12, the first magnetic mode is shifted upward in frequency toward the first electric mode. It is important to recognize that dielectric inclusions of this type have been used previously for bandwidth enhancements [28] and tuning purposes [29, 30].

The effects resulting from metal inclusions and air splits (or cutouts) on the dielectric resonator performance are illustrated pictorially in Fig. 13. (Specific design examples are provided in a subsequent section.) It is important to point out that, depending on the frequency range of interest, each of these designs offer different advantages in terms of ease of manufacturing, losses, and electrical size. For example, at microwave frequencies a resonator with a dipole insert may be fairly easy to realize, without a significant deterioration in the loss performance. The reasonable maintenance of the loss performance, together with the fact that the electric size of the resonator becomes smaller as the electric mode is downshifted to lower frequencies (ultimately overlapping the magnetic resonance), are clear advantages of this type of design. On the other hand, as the frequency is increased, lower-loss perturbations such as air inclusions may become a more attractive option.

3.1.1. Dielectric Cuts

For a rectangular resonator operating in the first magnetic, or $TE_{11\delta}^z$, mode with a cutout at the center $x = 0$ (Fig. 12), the electric field in

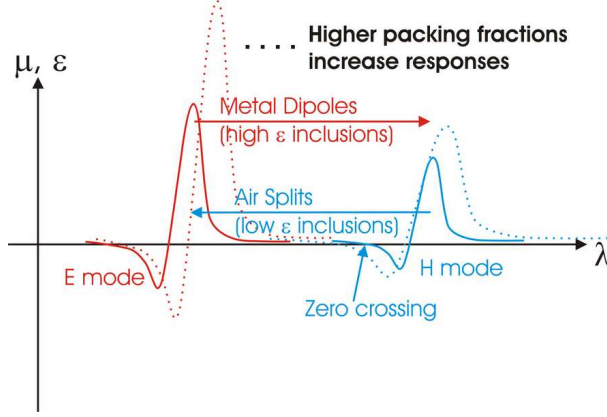


Figure 13. Illustration of resonance shifting due to metallic-dipole and air-split inclusions in the resonator. Also, as the packing fraction of the resonators is increased, the amplitudes of the responses are enhanced.

the local coordinate system is given by

$$\underline{E} = i\omega\mu_0 A \cos(k_z z) \cdot [\underline{e}_y k_x \sin(k_x x) \cos(k_y y) - \underline{e}_x k_y \cos(k_x x) \sin(k_y y)] \quad (21)$$

(note that in the local-coordinate system associated with the magnetic mode, for which H^{inc} is aligned with z , we take E^{inc} to be y directed so that it does not interact much with the $x = 0$ cutout). For this type of perturbed resonator design, we then have

$$\begin{aligned} \int_V \varepsilon \underline{E}_0 \cdot \underline{E}_0^* dV &\approx \mu_0 ab |A|^2 k^2 (k_x^2 + k_y^2) \int_{-c}^c \cos^2(k_z z) dz \\ &\approx \mu_0 abc |A|^2 k^2 (k_x^2 + k_y^2) \cdot \left[1 + \frac{\sin(2k_z c)}{2k_z c} \right] \end{aligned} \quad (22)$$

so that the numerator in the perturbation formula (corresponding to the air-split inclusion) becomes

$$\begin{aligned} \int_{V_p} (\varepsilon_p - \varepsilon) \underline{E}_p \cdot \underline{E}_0^* dV &\approx \Delta(\varepsilon_p - \varepsilon_2) (\varepsilon_2 / \varepsilon_p) \int_{-b}^b dy \int_{-c}^c |E_x(0, y, z)|^2 dz \\ &\approx \mu_0 \frac{\Delta b}{\varepsilon_p} (\varepsilon_p - \varepsilon_2) |A|^2 k^2 k_y^2 \int_{-c}^c \cos^2(k_z z) dz \\ &\approx -\mu_0 \Delta bc (\varepsilon_2 / \varepsilon_p - 1) |A|^2 k^2 k_y^2 \left[1 + \frac{\sin(2k_z c)}{2k_z c} \right] \end{aligned} \quad (23)$$

Finally we obtain

$$-\frac{\delta\omega}{\omega_0} \approx -\frac{\Delta}{2a} (\varepsilon_2 / \varepsilon_p - 1) \left(\frac{k_y^2}{k_x^2 + k_y^2} \right) \approx -\frac{\Delta}{2a} (\varepsilon_2 / \varepsilon_p - 1) \left(\frac{a^2}{a^2 + b^2} \right) \quad (24)$$

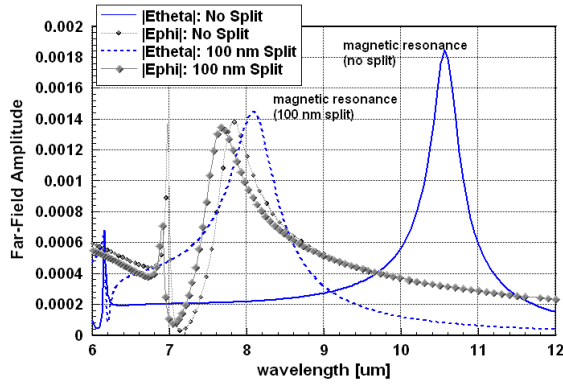


Figure 14. A comparison between the spectral positions of the electric and magnetic resonances for an unperturbed cubic resonator (in this case a PbTe cube with side length $1.53 \mu\text{m}$) and the same cubic resonator with a 100 nm gap positioned as shown in in Fig. 12. With a 100 nm gap, near-degeneracy between the lowest order electric and magnetic modes is realized.

where for the case of a cube ($a = b = c$) the normalized frequency shift becomes

$$-\frac{\delta\omega}{\omega_0} = -\frac{\Delta}{4a} (\varepsilon_2/\varepsilon_p - 1) \quad (25)$$

From the approximate waveguide model, the first magnetic mode occurs near the $TE_{11\delta}^z$ frequency $k_{11\delta}^z = \pi\sqrt{2.49}/(2a)$ and from the simulation we find that the first excited electric mode occurs near $TM_{\xi\xi 1}^z$ or $k_{\xi\xi 1} \approx \pi\sqrt{5}/(2a)$. Thus to obtain overlapping electric and magnetic modes, the desired shift is $\delta\omega/\omega_0 = \sqrt{5/2.49} - 1 \approx 0.42$ (for comparison, the numerical simulation for the first magnetic mode indicates that $\delta\omega/\omega_0 \approx 0.36$ is required). Using (25), this shift is realized with an air split of normalized thickness $\Delta/a \approx 0.054$ for the case of a cubic resonator of side length $1.53 \mu\text{m}$ and permittivities $\varepsilon_2 = 32\varepsilon_0$ and $\varepsilon_p = \varepsilon_0$. For comparison, we find from the simulation in Fig. 14 that with a normalized cutout of $\Delta/a \approx 0.07$, the magnetic resonance is shifted from about $10.6 \mu\text{m}$ to approximately $8 \mu\text{m}$. For this case of the air-split cube, we observe the electric resonance to shift slightly with the introduction of a split, but remain relatively fixed for all split dimensions thereafter.

If the rectangular resonator is split in half and the halves are separated by a region of ε_p (instead of a change of state of the material in the cutout) we need to include the magnetic energy for an introduced

volume rather than a change in the material state [20, 31]

$$-\frac{\delta\omega}{\omega_0} \approx \frac{\int_{V_p} \mu_0 \underline{H}_0^* \cdot \underline{H}_0 dV - \int_{V_p} \varepsilon_p \underline{E}_p^* \cdot \underline{E}_p dV}{2 \int_V \varepsilon \underline{E}_0 \cdot \underline{E}_0^* dV} \approx \frac{\Delta}{2a} \left[\left(1 - k_z^2/k^2\right) + \left(\frac{k_y^2}{k_x^2 + k_y^2}\right) \cdot \left\{ (k_z/k)^2 \left(1 - \frac{\sin(2k_z c)}{2k_z c}\right) \right\} / \left(1 + \frac{\sin(2k_z c)}{2k_z c}\right) - \varepsilon_2/\varepsilon_p \right] \quad (26)$$

(note that the tangential electric field for this first magnetic mode vanishes at the cutout). Thus, we find for an $\varepsilon_2 = 32\varepsilon_0$ cube with $k_x^2 = k_y^2$, $2k_z c \approx 0.7017\pi$ and $k = \pi\sqrt{2.49}/(2a)$ that

$$-\frac{\delta\omega}{\omega_0} \approx \frac{\Delta}{4a} (1.696 - \varepsilon_2/\varepsilon_p) \quad (27)$$

This result is similar to that of the sphere given in [20] and not too much different from the original estimate (25) (where we changed the state of the material in the split).

It is important to note that for the rectangular resonator (as shown in [20] for the spherical resonator), the wavelength shift in the position of the magnetic resonance decreases as the thickness of the cutout is increased and eventually saturates to the magnetic resonance spectral position associated with the half-resonator structure. This effect will be discussed in further detail in the next section. Numerical simulations for a variety of cutout thicknesses will also be presented.

3.1.2. Normal Electric Field in Cutouts (Shift Saturation)

An impedance boundary condition can be constructed to describe the cutouts in a manner that in some cases is simpler and allows a level of analytical treatment of the structural response to the presence of the cutouts. The boundary condition is easily derived by taking the electric field to be quasistatic in the cutout such that $\underline{E} = -\nabla V_e$, $\nabla^2 V_e = 0$, and $V_e \approx -f_0(\underline{t}) - n f_1(\underline{t})$, where the local tangent vector to the cutout is \underline{t} , and the local normal coordinate is n . $f_j(\underline{t})$, $j = 1, 2$ are both slowly varying in \underline{t} compared to the distance Δ and can thus be taken locally as constants, and $E_n \approx f_1$. The boundary condition can thus be written as a jump in the tangential electric field (or magnetic current) over split thickness Δ , where the jump is proportional to the tangential derivative of the normal field at the split. Thus, we have

$$-\underline{K}_m = \underline{n} \times (\underline{E}^+ - \underline{E}^-) = \left(\frac{\Delta\varepsilon_2}{2\varepsilon_p}\right) \underline{n} \times \nabla_t [\underline{n} \cdot (\underline{E}^+ + \underline{E}^-)] \quad (28)$$

This boundary condition immediately gives an estimate on how thick a cutout can be before the structural response to the perturbation must be included in the normal field.

The analysis for the rectangular resonator is somewhat easier than for the sphere [20] because a constant thickness cut conforms with the rectangular geometry of the rectangular resonator; further simplification is used here (because of the complicated interior-exterior boundary value problem of the rectangular resonator) by considering only the interior resonator problem with PMC walls. Thus for a rectangular resonator using an interior PMC approach, starting with the TE_{110}^z mode instead of $TE_{11\delta}^z$ and using the TE_{n10}^z modes to match the impedance boundary condition at the split, we find that the normal field in the split is

$$\begin{aligned}
 E_n = E_x(x=0) &\approx -i\omega\mu_0 A \frac{\varepsilon_2}{\varepsilon_p} k_y \sin(k_y y) \cdot \left[1 - \left(\frac{\Delta\varepsilon_2}{\varepsilon_p} \right) \left(\frac{a}{2} \right) k_y^2 + \dots \right] \\
 &\approx E_x^{(0)}(x=0) \frac{\varepsilon_2}{\varepsilon_p} / \left[1 + \left(\frac{\Delta\varepsilon_2}{\varepsilon_p} \right) \left(\frac{a}{2} \right) \left(\frac{\pi}{2b} \right)^2 + \dots \right] \quad (29)
 \end{aligned}$$

where $E_x^{(0)}$ is the field without the perturbation being present. Note here that the cutout is at $x = 0$, and E^{inc} is y directed so it does not interact much with the perturbation. Although this result is not extremely accurate (due to the simplifications under which it was derived), it does demonstrate the frequency shift (if this normal field is inserted into the perturbation formula) resulting from a split thickness Δ and permittivity contrast $\varepsilon_2/\varepsilon_p$, as well as a ‘‘saturation’’ effect associated with the normal field. The saturation effect is observed in Fig. 15, where the numerically-simulated shift in the magnetic resonance is seen to lessen with increasing split size. Thus, if we examine the cube limit of (29), the normal field in the split becomes

$$E_n \approx E_x^{(0)}(x=0) \frac{\varepsilon_2}{\varepsilon_p} / [1 + (\varepsilon_2/\varepsilon_p) (\Delta/a) \pi^2/8 + \dots] \quad (30)$$

Furthermore, if we ignore any change in total energy in the perturbation formula, but change the numerator value due to this normal field change, we obtain

$$\frac{\delta\omega}{\omega_0} \approx \frac{\Delta}{4a} (\varepsilon_2/\varepsilon_p - 1) / [1 + c_1 (\varepsilon_2/\varepsilon_p - 1) (\Delta/a)] \quad (31)$$

(Here we used the same factor $\varepsilon_2/\varepsilon_p - 1$ in the denominator as the initial numerator factor (25). As with the spherical resonators discussed in [20], it is interesting that we can match the widely-spaced half resonator (in this case, the half-cube) by resetting c_1 . A cube with dimension $2a = 1.53 \mu\text{m}$, $\varepsilon_2 = 32\varepsilon_0$, and $\varepsilon_1 = \varepsilon_0$ has resonant wavenumber from the waveguide formula $k_{11\delta} \approx \pi\sqrt{2.49}/(2a)$ or a wavelength $\lambda_0 \approx 10.97 \mu\text{m}$. If this cube is split in half ($b \rightarrow b/2$), each half has a resonant wavenumber predicted from the waveguide

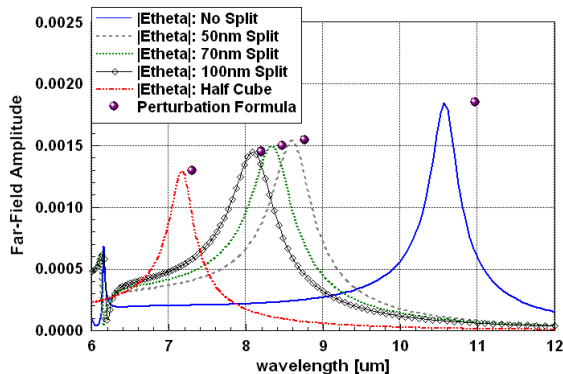


Figure 15. As the split in the cubic resonator ($s = 1.53 \mu\text{m}$) is increased, the shift in the magnetic resonators saturates to the half-cube magnetic resonance limit. For comparison, the wavelength shifts predicted via the perturbation formula are shown for the cases of the unperturbed cubic resonator, a cube with a 50 nm, 70 nm, and 100 nm cutout, as well as a half-cube resonator (note that the ordinate values associated with the points have been selected arbitrarily to place them in the vicinity of the resonant peaks of the simulations).

approximation $k_{11\delta} \approx \pi\sqrt{5.61}/(2a)$ or a wavelength $\lambda_0 \approx 7.3 \mu\text{m}$. Hence from the waveguide formula we expect a saturation value of $\delta\omega/\omega_0 \rightarrow \sqrt{5.61/2.49} - 1 \approx 0.50$, which requires us to change the coefficient to

$$c_1 \rightarrow 0.5 \quad (32)$$

Finally, formula (31), constant (32), and the waveguide value for ω_0 with $\varepsilon_p = \varepsilon_0$ are used to predict the position of the shifted magnetic resonance. These frequency predictions are shown as points in Fig. 15, with the far-field amplitudes (ordinate axis) having been arbitrarily chosen to occur near the resonant peaks of the simulation. (The scattering results associated with the numerical simulation of an isolated rectangular resonator with different split sizes are shown with varying line types.) The initial error results from the error in the simple waveguide prediction for the unperturbed resonance. This can be eliminated by using the simulation values, but as a design tool based purely on the analytical results, this is useful as it stands.

3.2. Combining Perturbation Effects

This subsection discusses combining perturbations for the purpose of: 1) enabling operation further from the resonant peaks and consequently

enabling loss reductions, 2) overcoming the shift saturation discussed in the previous section and allowing smaller individual inclusions to be used, and in the final case, 3) making the resulting design somewhat invariant with respect to incident plane-wave angle.

3.2.1. Inclusion and Packing

In order to allow flexibility in precise alignment of the modal resonances, as well as to operate further away from the large losses associated with the resonant peak region, the responses in a lattice of perturbed resonators (including either dipole inclusions or air splits, for example) can be boosted by using a larger volume-packing fraction. An example of a periodic-array of cubic dielectric resonators is shown in Fig. 16. With the extra degree of freedom associated with the lattice arrangement (versus the single-resonator response), it is possible, for example, to achieve negative index in the tail regions of the two resonances where the losses are lower. While results showing packing effects on the loss performance of degenerate all-dielectric resonator designs will be presented in a follow-on effort, increases in the packing fraction is shown to decrease the loss associated with a metal-core, dielectric-shell spherical design in [16].

3.2.2. Air Split and Metallic Decorations

If minimizing the size of the perturbations is of interest (in accordance with fabrication issues or loss considerations, for example), perturbations can be combined so as to simultaneously frequency shift the magnetic and electric resonances toward each other and ultimately realize overlap at some intermediate frequency to the fundamental ones. We note that in the approaches discussed previously, one inclusion type was employed to selectively frequency shift one resonance while leaving the other unperturbed. Figure 17 shows a

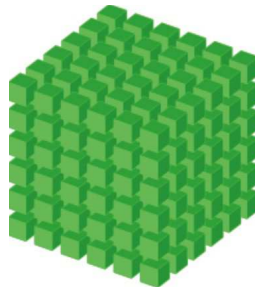


Figure 16. A periodic array of dielectric cubic resonators.

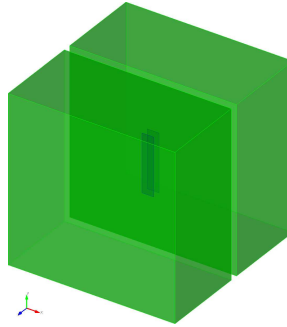


Figure 17. A dual-perturbation cubic resonator design that uses an air split together with metallic-strip dipoles (on each face of the split) to realize modal degeneracy.

rectangular resonator design that includes an air split used to interact with the lowest-order magnetic resonance plus two strip dipoles placed on each face of the split for interaction with the lowest-order electric resonance. Here modal degeneracy is obtained by orienting the air split perpendicular to the direction of propagation (and parallel to the plane containing the incident plane-wave polarizations \vec{H} and \vec{E}), orienting the strip dipoles along the direction of the incident electric field \vec{E} , and choosing the appropriate split-thickness and dimensions of the dipole to realize the desired frequency shifts.

Advantages of the dual-perturbation design, such as that shown in Fig. 17, are that the electrical size of the resonator is kept smaller versus the single air-split design (since alignment of the resonances occurs at an intermediate frequency rather than at the higher frequency of the fundamental electric resonance characterizing the unperturbed rectangular resonator) and that the saturation effect discussed in Section 3.1.2 is circumvented. It is important to recognize however, that for higher-frequency operation where losses associated with the metallic dipoles may not be tolerable, the multiple-perturbation designs discussed in the next two sections may be preferable.

3.2.3. Air Split and Aspect Ratio

As an alternative to the cubic-resonator designs that have been discussed thus far, the aspect ratio of the resonators can also be manipulated (going from cubic to rectangular) to help bring about modal degeneracy. More specifically, a slight elongation in the incident magnetic field direction results in a wavelength upshift of the electric resonance but yields less of an upshift (in wavelength) of the magnetic resonance (since the magnetic field already penetrates the exterior

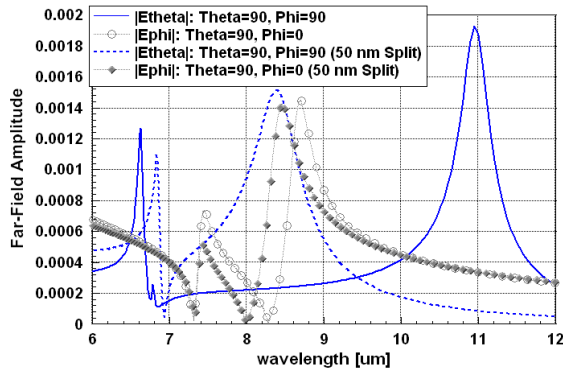


Figure 18. A cubic PbTe resonator is stretched along the direction of the incident magnetic field to realize a wavelength upshift in the electric resonance and a cut is introduced along the direction of propagation to yield a wavelength downshift in the magnetic resonance.

region in this direction). This approach can thus be used to progress toward resonance alignment (since the magnetic resonance already existed at a longer wavelength than the electric resonance). Combining this perturbation effect with that accompanying an air-split inclusion (which can be used to further downshift the magnetic resonance in wavelength) provides a path towards an alternative degenerate resonator design. Figure 18 shows the simulation results for a slightly elongated PbTe resonator (the side lengths of the resonator in the y and z -directions are $s = 1.53 \mu\text{m}$, while the length along the x -direction of the incident H field is $s_x = 1.91 \mu\text{m}$) and containing a single air split of 50 nm. Thus, with the elongation of the cube together with a relatively minor cut perturbation, modal degeneracy is observed (for this design degeneracy occurs at $\lambda \approx 8.3 \mu\text{m}$). The electric resonance position has been shifted upward in wavelength from its original position of $7.8 \mu\text{m}$ (Fig. 7) to $8.7 \mu\text{m}$ due to the stretching of the cube in the x -direction (along the direction of the incident H field) but moves down slightly in wavelength with the introduction of the air split. For comparison, we note that in using a cubic resonator geometry ($1.53 \mu\text{m}$ for all sides), an air split of over 150 nm is necessary to achieve modal alignment (however, by this point saturation in the shifting of the magnetic resonance becomes a significant factor). It is also important to point out that although further increasing the aspect ratio of the cube (here we have used an aspect ratio of 1.25) does lead to greater shifts in the electric resonance, our goal with these designs is to keep the size of the resonators down with the combination of the elongation and the split perturbation so as to remain in the effective-media limit.

3.2.4. Multiple Cuts (Dielectric Anisotropy)

We have also observed that the modal-shifting limitations discussed in Section 3.1.2 can be overcome by introducing multiple air splits in the dielectric resonator. Multiple air-split spherical designs are discussed in [20, 21]; in a similar manner, rectangular resonators split in the cross section perpendicular to the incident electric field can be used to realize a greater tuning range (beyond the saturation limit inherent to the single air-split approach). A multiple air-split rectangular design with cuts in the cross section denoted by the local x - y plane with the incident electric field oriented along the local z direction (that is, cuts in the local x - z and y - z planes) is shown in the leftmost part of Fig. 19. It is important to recognize that an additional advantage of this approach, besides overcoming saturation limitations, is that the resonator response becomes more independent of the azimuthal angle of incidence (for a spherical resonator with many cuts [20, 21], the response becomes independent of azimuthal angle of incidence).

In the specialized case of a rectangular resonator with a square cross section perpendicular to the incident electric field direction, the symmetries can be further used to cut the dielectric along the diagonals since there is no normal electric field with respect to these additional

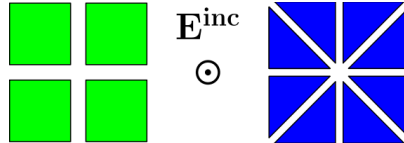


Figure 19. Air-split perturbations are introduced in the cross section of a rectangular dielectric resonator to realize more flexibility in the tuning range of the magnetic resonance. In the case that the resonator has a square cross section, diagonal cuts can also be introduced.

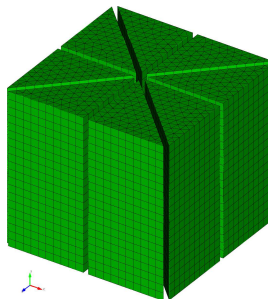


Figure 20. A three-dimensional view of the four-cut cube geometry shown in Fig. 19.

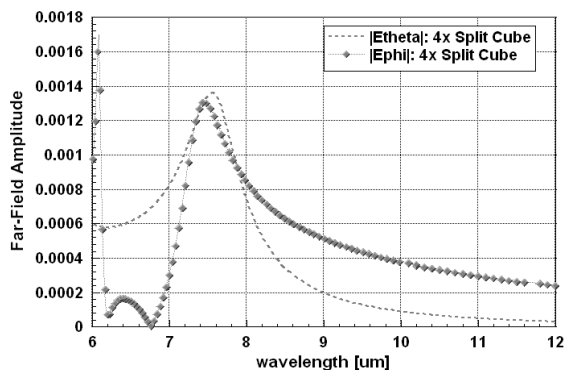


Figure 21. With the introduction of four air splits (of 50 nm each) in a cubic PbTe resonator of side length $s = 1.53 \mu\text{m}$, modal degeneracy of the two lowest-order modes is realized and the second magnetic mode is pushed away from the degenerate frequency.

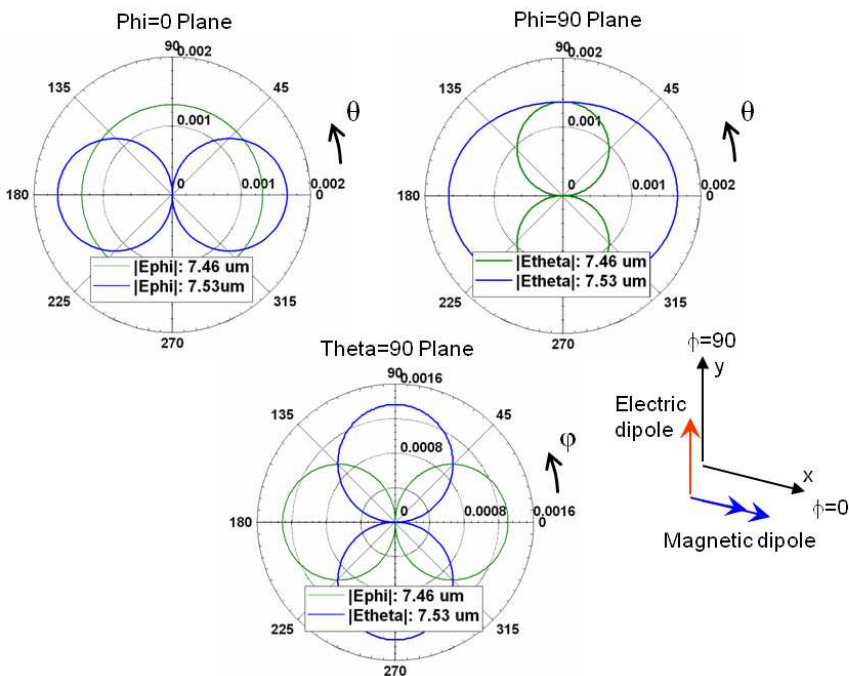


Figure 22. The scattered patterns associated with a four-cut cubic PbTe resonator ($s = 1.53 \mu\text{m}$) with 50 nm gaps. The patterns are sampled at each of the peak frequencies determined from the results in Fig. 21.

cuts for the first electric mode by virtue of the relation

$$\underline{E}_t = \nabla_t \left(\frac{\partial \psi_e}{\partial z} \right) \quad (33)$$

(here we have evenness of the mode about the diagonals of the square and $\nabla_t = \underline{e}_x \partial / \partial x + \underline{e}_y \partial / \partial y$). We thus arrive at split-rectangular resonators as shown in Figs. 19 and 20.

Four-split rectangular resonator designs also have the advantage that the second magnetic mode will be further displaced from the degenerate frequency of the two lowest-order modes; this can be observed by comparing results in Fig. 14 where this mode is located at approximately $7.0 \mu\text{m}$ to those in Fig. 21 where the second magnetic mode occurs at about $6.1 \mu\text{m}$. Fig. 21 also demonstrates that with the inclusion of four air splits of 50 nm thickness, alignment between the magnetic and electric modes is seen to occur at approximately $7.5 \mu\text{m}$. Realizing further separation between these modes is worth acknowledging since suppressing this higher-order mode near the operating frequency means that additional losses are not incurred. To verify the dipole nature of the modes in the four-split design, the scattered patterns at the two-lowest order resonances are presented in Fig. 22.

4. CONCLUSIONS

This paper discusses an approach for tuning resonances in rectangular dielectric resonators which can then be used to construct single-particle, negative-index metamaterials. In particular, high-contrast inclusions in the form of metallic dipoles are employed to shift the first electric resonance down (in frequency) to the first magnetic resonance, or alternatively, air splits are used to shift the first magnetic resonance up (in frequency) near the first electric resonance. Degenerate dielectric designs become especially useful in infrared or visible-frequency applications where the resonator sizes associated with the lack of high-permittivity materials can become sufficiently large to enable propagation of higher-order lattice modes in the resulting medium.

Cavity-perturbation theory has been used to initially motivate the types of perturbations within the dielectric resonators (including the polarization and placement) that would provide the necessary modal shifts, and finally to arrive at simple formulas that can be used for degenerate-resonator design. Alternative designs, each with different advantages varying from minimizing the electrical size to minimizing loss mechanisms, have been presented. Multiple-perturbation designs in particular have been shown to allow for the

tuning of the first-order magnetic resonance clear past the frequency of the first electric resonance and thus make the accessibility to negative-index metamaterials that adhere to effective-media limits much more promising.

ACKNOWLEDGMENT

Sandia National Laboratories is a multi-program laboratory managed and operated by Sandia Corporation, a wholly owned subsidiary of Lockheed Martin Corporation, for the U.S. Department of Energy's National Nuclear Security Administration under contract DE-AC04-94AL85000.

REFERENCES

1. Tretyakov, S., *Analytical Modeling in Applied Electromagnetics*, Artech House, 2003.
2. Smith, D. R. and J. B. Pendry, "Homogenization of metamaterials by field averaging," *J. Opt. Soc. Am. B*, Vol. 23, No. 3, Mar. 2006.
3. Lerat, J. M., N. Mallejac, and O. Acher, "Determination of the effective parameters of a metamaterial by field summation method," *Journal of Appl. Phys.*, Vol. 100, 084908, 2006.
4. Liu, R., R. J. Cui, D. Huang, B. Zhao, and D. R. Smith, "Description and explanation of electromagnetic behaviors in artificial metamaterials based on effective medium theory," *Physical Review E*, Vol. 76, 026606, 2007.
5. Koschny, T., P. Markos, E. N. Economou, D. R. Smith, D. C. Vier, and C. M. Soukoulis, "Impact of inherent periodic structure on effective medium description of left-handed and related metamaterials," *Physical Review B*, Vol. 71, 245105, 2005.
6. Belov, P. A. and C. R. Simovski, "On homogenization of electromagnetic crystals formed by uniaxial resonant scatterers," *Physical Review E*, Vol. 72, 026615, 2005.
7. Pendry, J. B., A. J. Holden, D. J. Robbins, and W. J. Stewart, "Magnetism from conductors and enhanced nonlinear phenomena," *IEEE Trans. Microwave Theory and Tech.*, Vol. 47, No. 11, Nov. 1999.
8. Tretyakov, S., S. Maslovski, and P. Belov, "An analytical model of metamaterials based on loaded wire dipoles," *IEEE Trans. on Antennas and Propag.* Vol. 51, 2562, 2003.
9. Tretyakov, S., "Meta-materials with wideband negative permittiv-

- ity and permeability,” *Microwave and Optical Technology Letters*, Vol. 31, No. 3, 163, 2001.
10. Basilio, L. I., L. K. Warne, W. L. Langston, W. A. Johnson, and M. B. Sinclair, “A quick and easy simulation procedure to aid in metamaterial unit-cell design,” *IEEE Antennas Wireless Propag. Lett.*, Vol. 10, 1567–1570, 2011.
 11. Simovski, C. R. and S. A. Tretyakov, “Model of isotropic resonant magnetism in the visible range based on core-shell clusters,” *Phys. Rev. B*, Vol. 79, 045111, 2009.
 12. Kim, J. and A. Gopinath, “Simulation of metamaterial containing cubic high dielectric resonators,” *Phys. Rev. B*, Vol. 76, 115126, 2007.
 13. Popa, B. and S. Cummer, “Compact dielectric particles as a building block for low-loss magnetic materials,” *Phys. Rev. Lett.*, Vol. 100, 207401, 2008.
 14. Sinclair, M., J. Ginn, J. Wendt, J. Stevens, D. Peters, L. Basilio, L. Warne, P. Clem, and J. Ihlefeld, “All dielectric infrared metamaterial,” *SPIE Optics + Photonics*, Paper 8093-44, 2011.
 15. Kuester, E., N. Memic, S. Shen, A. D. Scher, S. Kim, K. Kumley, and H. Loui, “A negative refractive index metamaterial based on a cubic array of layered nonmagnetic spherical particles,” *Progress In Electromagnetics Research B*, Vol. 33, 175–202, 2011.
 16. Basilio, L., L. Warne, W. Langston, W. Johnson, and M. Sinclair, “A negative-index metamaterial design based on metal-core, dielectric shell resonators,” *IEEE Antennas and Propagation Society International Symposium*, Spokane, Washington, USA, 2011.
 17. Ahmadi, A. and H. Mosallaei, “Physical configuration and performance modeling of all-dielectric metamaterials,” *Phys. Rev. B*, Vol. 77, Art. 045104, 2008.
 18. Jylha, L., I. Kolmakov, S. Maslovski, and S. Tretyakov, “Modeling of isotropic backward-wave materials composed of resonant spheres,” *J. Appl. Phys.*, Vol. 99, Art. 043102, 2006.
 19. Palik, E., *Handbook of Optical Constants and Solids*, Academic, Orlando, Fla., 1986.
 20. Warne, L. K., L. I. Basilio, W. L. Langston, W. A. Johnson, and M. B. Sinclair, “Perturbation theory in the design of degenerate spherical dielectric metamaterial resonators,” Sandia National Laboratories Internal Report, 2011.
 21. Basilio, L. I., L. K. Warne, W. L. Langston, W. A. Johnson, and M. B. Sinclair, “Microwave-frequency, negative-index

- metamaterial designs based on degenerate dielectric resonators,” *IEEE Antennas Wireless Propag. Lett.*, Vol. 11, 113–116, 2012.
22. Johnson, W., L. Basilio, J. Kotulski, R. Jorgenson, L. Warne, R. Coats, D. Wilton, N. Champagne, F. Capolino, J. Grant, and M. Khayat, “Eiger: An open-source frequency domain electromagnetics code,” *IEEE Antennas and Propagation Society International Symposium*, Honolulu, Hawaii, USA, 2007.
 23. Van Bladel, J., “On the resonances of a dielectric resonator of very high permittivity,” *IEEE Trans. on Microwave Theory and Tech.*, Vol. 23, No. 2, 199–208, Feb. 1975.
 24. Van Bladel, J., “The excitation of dielectric resonators of very high permittivity,” *IEEE Trans. on Microwave Theory and Tech.*, Vol. 23, No. 2, 208–217, Feb. 1975.
 25. Mongia, R. and A. Ittipiboon, “Theoretical and experimental investigations on rectangular dielectric resonator antennas,” *IEEE Trans. on Antennas and Propag.*, Vol. 45, No. 9, 1348, 1997.
 26. Harrington, R. F., *Time-harmonic Electromagnetic Fields*, 317–326, McGraw-Hill Book Company, New York, 1961.
 27. Lin, X. Q., T. J. Cui, J. Y. Chin, X. M. Yang, Q. Cheng, and R. Liu, “Controlling electromagnetic waves using tunable gradient dielectric metamaterial lens,” *Applied Phys. Lett.*, Vol. 92, 131904, 2008.
 28. Antar, Y. M. M. and D. Guha, “Composite and hybrid dielectric resonator antennas: Recent advances and challenges,” *23rd National Radio Science Conference*, Menoufiya University, Egypt, Mar. 14–16, 2006.
 29. Poplavko, Y. M., Y. P. Prokopenko, V. I. Molchanov, and A. Dogan, “Frequency-tunable microwave dielectric resonator,” *IEEE Trans. on Microwave Theory and Tech.*, Vol. 49, No. 6, 2001.
 30. Derneryd, A., U. M. Khan, A. A. Kishk, M. Milutinovic, and P. Persson, “Dual-polarized dielectric resonator antennas for base station applications,” *5th European Conference on Antennas and Propagation*, Rome, Italy, 2011.
 31. Borginis, F. E. and C. H. Papas, *Electromagnetic Waveguides and Resonators*, Hanbuch Der Physik, S. Flugge, Editor, Vol. XVI, 411–414, Springer-Verlag, Berlin, 1958.